



OPEN

Advanced modeling of salt-inducible kinase (SIK) inhibitors incorporating protein flexibility through molecular dynamics and cross-docking

Jorge Luis Valdés-Albuernes, Erbio Díaz-Pico, Sergio Alfaro & Julio Caballero

Salt-inducible kinases (SIK1, SIK2, and SIK3) regulate metabolism and immune responses, making them promising targets for inflammatory and autoimmune diseases. Understanding inhibitor selectivity among isoforms is crucial for therapeutic development. In this study, 44 compounds were investigated as SIK inhibitors using molecular modeling. A flexible treatment of the kinases via molecular dynamics (MD) simulations captured binding site conformational changes, followed by molecular docking to generate protein kinase (PK)-ligand complex models. Ligand orientations were validated against crystallographic data using LigRMSD and interaction fingerprints (IFPs). A genetic algorithm was applied to select conformations that maximize correlation between docking energies and biological activities, yielding R^2 values of 0.821, 0.646, and 0.620 for SIK1, SIK2, and SIK3, respectively. Our results highlight the importance of protein flexibility in achieving accurate correlations between docking energies and experimental pIC_{50} values, enhancing inhibitor selectivity predictions.

Keywords Salt-Inducible kinase, SIK inhibitors, Docking energy-activity correlation, Flexible molecular Docking, Molecular dynamics

Salt-inducible kinases (SIK1, SIK2, and SIK3) are a subfamily of serine/threonine kinases belonging to the AMPK (AMP-activated protein kinase) family, and they play an essential role in regulating critical cellular processes such as energy metabolism, gene transcription, and stress response¹. At the cellular level, SIKs are involved in metabolic processes such as gluconeogenesis and steroidogenesis, regulating glucose and lipid homeostasis in response to hormonal and environmental signals^{2,3}. They also regulate cellular immune responses, inflammation, and sleep/circadian rhythms^{4,5}.

SIKs have prominent roles in several pathologies, including metabolic diseases, cancer, and inflammatory diseases^{6,7}. Their involvement in pro-inflammatory pathways and immunoregulation, opening new opportunities for the development of therapeutic strategies aimed at modulating immune responses^{8,9}. It has been demonstrated that SIK inhibition has effects on inflammatory pathways, as these protein kinases (PKs) regulate both innate and adaptive immune cells. The role of SIKs in inflammatory diseases has driven the development of inhibitors that can block their functions in the immune system^{10–12}. In the context of immune responses, SIK inhibition has shown promise as a strategy to modulate both innate and adaptive immunity, as it regulates the activation of macrophages and other immune cells. Therefore, it has been proposed that SIK inhibitors could be useful in treating chronic inflammatory diseases such as rheumatoid arthritis, ulcerative colitis, and other autoimmune disorders^{8,13}.

The design of selective inhibitors is crucial due to the differentiated function of SIKs in various tissues and immune system cells. There are many examples that demonstrate distinct biological roles for SIKs. For instance, evidence has been reported showing the complex roles of SIKs in various types of cancer. SIK1 exhibits tumor-suppressing functions and also links the PK LKB1 (liver kinase B1) to p53-dependent anoikis suppressing metastasis¹⁴. SIK2 is overexpressed in ovarian cancer, serving as an indicator of poor prognosis, and appears in advanced stages of gastric cancer^{15,16}. Additionally, it is associated with cell survival and tumor progression in

Centro de Bioinformática, Simulación y Modelado (CBSM), Facultad de Ingeniería, Universidad de Talca, 2 Norte 685, Talca, Chile. email: jcaballero@utalca.cl

lymphomas¹⁷. SIK3 is linked to inflammation processes in breast cancer and regulates the subcellular localization and activity of HDAC4 in leukemia^{6,18}. Designing selective SIK inhibitors can be used as chemical tools to clarify these distinct roles. Evidence suggests that selective pharmacology targeting SIK isoforms can offer benefits. It has been reported that SIK2 and SIK3 play a more significant role in immune cells. For example, both isoforms are required for Interleukin-33-dependent cytokine secretion¹⁹. Additionally, they have been observed as the primary isoforms in T cells⁴. On the other hand, SIK1 has a less prominent role in immune cells but is crucial in regulating blood pressure and vascular remodeling²⁰. Therefore, selectively inhibiting SIK2 and SIK3 while sparing SIK1 could minimize cardiovascular impact while maintaining the desired immune activity, compared to pan-SIK inhibition.

In recent years, several SIK inhibitors have been reported. Highly potent compounds such as HG-9-91-01 (Fig. 1A) and YKL-05-099 have provided valuable insights into the biological functions of SIKs^{21,22}; however, though their limited selectivity across isoforms and other PKs restricts their utility. Additional classes of potent pan-SIK inhibitors have been developed to further explore SIK physiology⁵. Bosutinib (Fig. 1B) and dasatinib, both approved for clinical use as PK inhibitors, are capable of inhibiting SIK activity at nanomolar levels²³. Although some series of SIK inhibitors have already been developed, there is still much work to be done to refine their selectivity and efficacy. For instance, very recently Peixoto, Desroy, and colleagues reported a series of SIK inhibitors in two articles. In the first article (whose compounds we will refer to as series A), they highlighted compound A_28 (GLPG3312), a potent nanomolar pan-SIK inhibitor¹². In the second article (whose compounds we will refer to as series B), they highlighted compound B_32 (GLPG3970), a selective dual SIK2/SIK3 inhibitor with nanomolar activity against these isoforms¹¹. In addition, authors co-crystallized the compound A_22 with SIK3 (PDB with code 8OKU; Fig. 1D, E), providing initial material to investigate the orientations in the other isoforms and explain which structural characteristics of the PK-inhibitor complexes contribute to selectivity. Compounds from series A and B are ATP-competitive PK inhibitors; it is well known that PKs share highly conserved ATP-binding pockets, so inhibitors targeting this site often have poor specificity. Therefore, understanding the characteristics that explain the differences in activity in such similar sites is not a trivial task.

The crystal structures of SIK3-inhibitor complexes have been instrumental in identifying which regions of the active site are occupied and could be targeted in the design of future selective compounds. Öster et al.²⁴ resolved the structures of SIK3 in complex with HG-9-91-01 (PDB: 8R4V), bosutinib (8R4Q), and MR1A9 (8R4U). Together with the previously reported structure of the A_22-SIK3 complex (8OKU), relevant information about these complexes is shown in Fig. 1. SIK3 features a typical ATP-binding site common to PKs, where residue A145 in the hinge region forms one or two hydrogen bonds (HBs) with the ligands. The compounds also interact near the gatekeeper residue T142, the hinge residue Y144, the catalytic lysine K95, the conserved glutamate E113 in

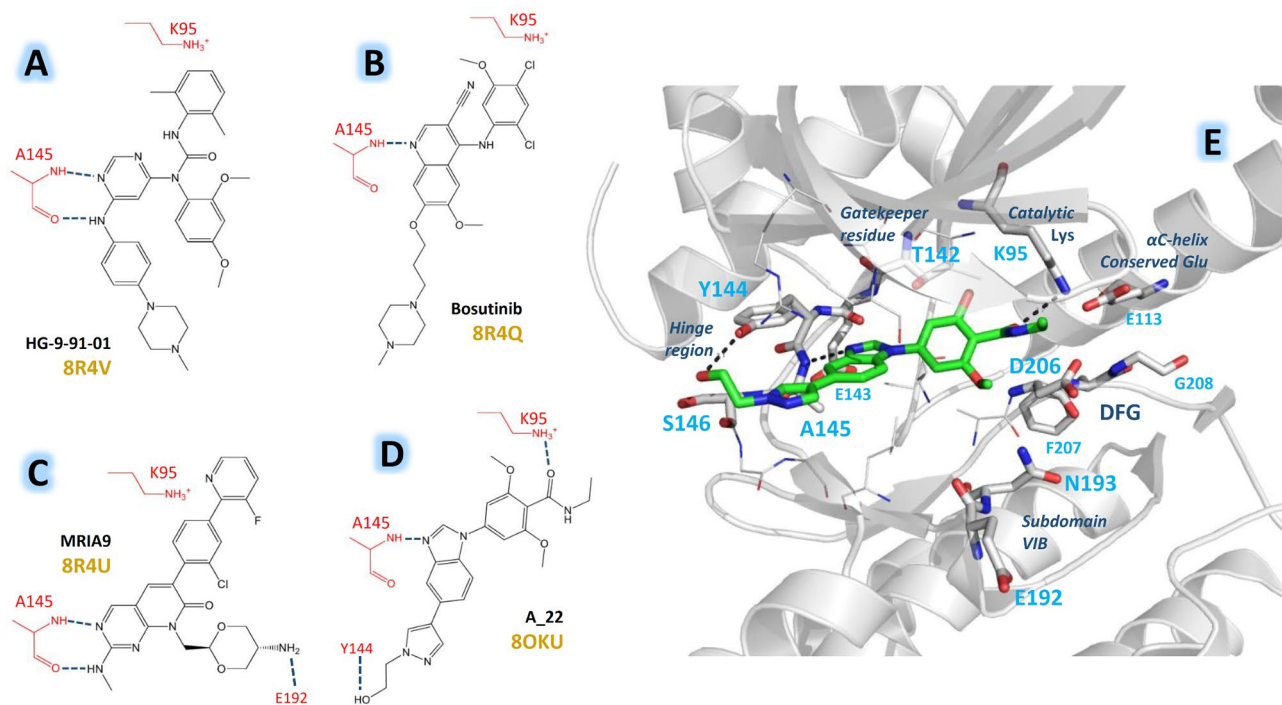


Fig. 1. Structures of inhibitors crystallized in complex with SIK3. Panels A–D show the structures of HG-9-91-01 (A), bosutinib (B), MR1A9 (C), and A_22 (D), highlighting their HBs with residue A145 in the hinge region of SIK3, the proximity to the catalytic lysine K95, and other observed HBs. The corresponding PDB codes for the complexes containing each compound are also indicated. Panel (E) shows the complex between A_22 (green sticks) and SIK3 (gray cartoon), depicting the different components of the binding site and the residues located in those regions (gray sticks).

the α C-helix, the DFG motif residue D206 (observed in the DFG-in conformation), and residues in subdomain VIB. Most of these residues are conserved in SIK1 and SIK2, making the structures of SIK3-inhibitor complexes highly valuable for studying SIKs using molecular simulation methods and in silico drug design.

The use of computational tools to study PK inhibitors has been essential in recent decades for understanding activity differences among congeneric compounds^{25–33} and exploring the interactions of known molecules to support the design of new inhibitors^{34–39}. Recent studies have employed molecular modeling approaches to investigate the binding of various SIK inhibitors. For instance, computational analysis of the interaction between dasatinib and SIK2 revealed strong binding affinity, with molecular docking and molecular dynamics (MD) simulations suggesting structural regions suitable for optimization in future inhibitor design⁴⁰. In a separate study, MD simulations were used to investigate the multiple conformational states of the bosutinib–SIK2 complex, highlighting the conformational plasticity of the active site and the key role of hydrophobic interactions in ligand recognition⁴¹. Additionally, curcumin was recently modeled in complex with SIK3, where MD simulations indicated that its binding was stabilized by several key residues within the PK active site⁴². Together, these works underscore the relevance of molecular modeling techniques in elucidating the structural basis of SIK inhibition. In this work, we addressed the study of inhibitors from series A and B using molecular modeling tools. In total, series A and B contain 44 compounds^{11,12}. A protocol that uses computational methods, such as molecular docking and molecular dynamics (MD) simulations, was applied to find models containing the poses of all compounds, with docking energy values correlated with inhibitory activities, considering conformational changes in the binding sites of the three SIK isoforms. Through the analysis of our results, we identified subtle differences in the structures of the complexes between SIKs and the inhibitors that could be considered in the future design of selective SIK inhibitors.

Materials and methods

Preparation of the SIK inhibitors

The compounds were labeled with the letters A and B to differentiate their sources, followed by the compound's identifier in the respective article (compounds from reference¹² are labeled as A_x, while those from reference¹¹ are labeled as B_x). The chemical structures for all the 44 SIK inhibitors are listed in Table 1. Visualization was carried out using the Maestro Molecular Editor (version 12.8.117, Schrödinger LLC, New York, NY, USA, 2021), while structural processing was performed with Maestro's LigPrep module. To determine the protonation states of the compounds, Epik⁴³ was employed under physiological conditions at a pH of 7.

Preparation of SIK structures

The atomistic coordinates of SIK3 in complex with the inhibitor A_22 were extracted from Protein Data Bank (PDB) with the code 8OKU. The structures of SIK1 and SIK2 were obtained by using AlphaFold3⁴⁴, with this SIK3 structure as the template. For docking calculations, the PDB structures were prepared using the Protein Preparation Wizard module (Schrödinger LLC, New York, NY, USA, 2021). This process included removing crystallographic water molecules, assigning neutrality or charges to protonatable groups as appropriate, and performing restrained minimizations of the SIK protein models. Minimizations were carried out using the OPLS3 force field⁴⁵, applying a harmonic restraint of 25 kcal mol^{−1} Å^{−2} to heavy atoms, while hydrogen atoms remained unrestrained. The heavy atoms were minimized until reaching a root-mean-square deviation (RMSD) of 0.3 Å.

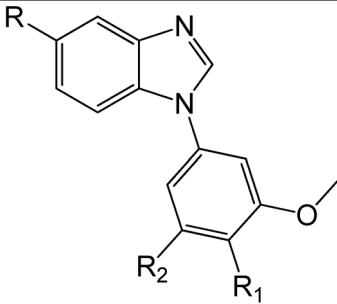
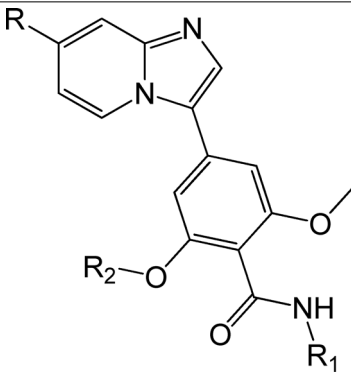
Docking calculations

Docking calculations were performed using Glide⁴⁶ to model ligand binding to the ATP-binding pockets of SIK1, SIK2, and SIK3. For each target protein, a cubic docking grid of 20 × 20 × 20 Å³ was defined, centered on the centroid of the co-crystallized ligand A_22 in SIK3 (8OKU). The selected box size was found to be sufficient to accommodate the diverse ligand sizes in our dataset, ensuring full coverage of the binding pocket.

Docking was carried out using both the standard precision (SP) and extra precision (XP) modes, with XP results primarily used for downstream analysis due to their higher accuracy in pose prediction⁴⁷. Each ligand was docked flexibly, while the receptor was kept rigid. For each compound, the top ten poses were retained based on GlideScore, and RMSD values were computed relative to the binding orientation observed in the reference structure. The optimal binding pose was selected by balancing the lowest docking energy with a reasonable RMSD to known or expected binding orientations.

LigRMSD

Docking similar inhibitors should result in binding modes that align closely with those observed in co-crystallized structures of SIK proteins. Accordingly, the studied ligands are expected to adopt comparable orientations when evaluated relative to one another. To validate the alignment of the docked orientations, we utilized the LigRMSD method⁴⁸. This approach identifies the maximum common substructure shared between a target compound and a reference molecule, then calculates the RMSD for the matching atoms. The relevance of the RMSD value depends on high values for both '%RefM' and '%MolM', which indicate the structural similarity between the compounds being compared. Specifically, '%RefM' represents the proportion of the reference molecule's atoms included in the overlap, while '%MolM' reflects the proportion of the docked molecule's atoms included in the overlap. Together, these percentages provide a comprehensive measure of similarity. With LigRMSD, we assessed how well the docking poses of the studied compounds aligned with the pose of the reference structure, PDB 8OKU. Additionally, we compared the docking poses of all compounds against the docking pose of A_22, using it as a standard for orientation analysis.

A_8 – A_28, B_10						
				-pIC ₅₀ (M)		
Compound	R	R ₁	R ₂	SIK1	SIK2	SIK3
A_8	Br	-CONH ₂	H	-6.37	-6.52	-6.73
A_9	Br	-CONH ₂	OMe	-6.85	-7.01	-7.27
A_10	1-ethyl-1H-pyrazol-4-yl	-CONH ₂	OMe	-8.70	-9.05	-9.00
A_11	1-ethyl-1H-pyrazol-4-yl	-CO ₂ Me	OMe	-7.36	-7.84	-7.99
A_12	1-ethyl-1H-pyrazol-4-yl	-CH ₂ OH	OMe	-8.39	-8.62	-8.43
A_13	1-ethyl-1H-pyrazol-4-yl	-COOH	OMe	-7.58	-7.69	-7.91
A_14	1-ethyl-1H-pyrazol-4-yl	-CONHMe	OMe	-7.60	-7.98	-8.30
A_15	1-ethyl-1H-pyrazol-4-yl	-CONHEt	OMe	-7.69	-8.10	-8.54
A_16	1-ethyl-1H-pyrazol-4-yl	-CONHCH ₂ CF ₃	OMe	-7.97	-8.48	-8.85
A_17	1-ethyl-1H-pyrazol-4-yl	-CONH(cPr)	OMe	-8.09	-8.60	-8.89
A_18	1-ethyl-1H-pyrazol-4-yl	-CONH(tBu)	OMe	-5.40	-5.41	-5.40
A_19	1-ethyl-1H-pyrazol-4-yl	-CON(cPr)Me	OMe	-6.12	-6.22	-6.79
A_20	1-ethyl-1H-pyrazol-4-yl	-CONHEt	OCHF ₂	-8.24	-8.64	-9.00
A_21	1-methyl-1H-pyrazol-4-yl	-CONHEt	OMe	-7.49	-7.95	-8.36
A_22	1-(2-hydroxyethyl)-1H-pyrazol-4-yl	-CONHEt	OMe	-7.67	-7.84	-8.38
A_23	1-(2-amino-2-oxoethyl)-1H-pyrazol-4-yl	-CONHEt	OMe	-7.70	-7.70	-8.18
A_24	1-(cyanomethyl)-1H-pyrazol-4-yl	-CONHEt	OMe	-7.84	-8.41	-8.66
A_25	1-(2-methoxyethyl)-1H-pyrazol-4-yl	-CONHEt	OMe	-7.50	-7.84	-8.17
A_26	1-(tetrahydro-2H-pyran-4-yl)-1H-pyrazol-4-yl	-CONHEt	OMe	-7.46	-8.04	-8.38
A_27	1-methyl-1H-pyrazol-4-yl	-CONHEt	OCHF ₂	-8.16	-8.48	-8.96
A_28 (GLPG3312)	1-methyl-1H-pyrazol-4-yl	-CONH(cPr)	OCHF ₂	-8.70	-9.16	-9.22
B_10	morpholino	-CONHCH ₂ CF ₃	OMe	-6.31	-6.93	-7.46
B_11 – B_27						
				-pIC ₅₀ (M)		
Compound	R	R ₁	R ₂	SIK1	SIK2	SIK3
B_11	Morpholino	-CH ₂ CF ₃	Me	-6.50	-7.25	-8.33
B_12	Morpholino	cPr	CHF ₂	-7.20	-7.80	-8.22
B_13	3,3-difluoroazetidin-1-yl	-CH ₂ CF ₃	Me	-6.77	-7.64	-8.50
B_14	3,3-difluoroazetidin-1-yl	cPr	CHF ₂	-7.57	-8.24	-8.77
B_15	4-methylpiperazin-1-yl	-CH ₂ CF ₃	Me	-6.16	-7.45	-7.96
B_16	4-methylpiperazin-1-yl	cPr	CHF ₂	-7.08	-8.27	-8.51
B_17	4-acetyl-piperazin-1-yl	cPr	CHF ₂	-7.35	-8.23	-8.85
B_18	4-(2-hydroxyethyl)piperazin-1-yl	cPr	CHF ₂	-7.21	-8.28	-8.72
B_19	4-(dimethylamino)piperidin-1-yl	cPr	CHF ₂	-7.77	-8.59	-8.77
Continued						

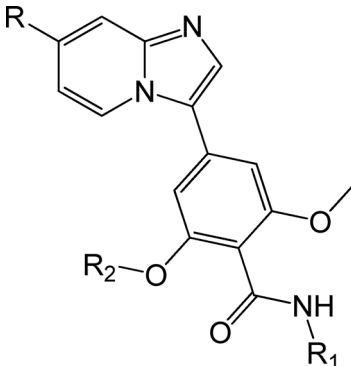
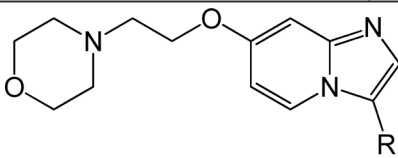
B_11 – B_27						
	Compound	R	R ₁	R ₂	-pIC ₅₀ (M)	
B_20		3-(dimethylamino)azetidin-1-yl	cPr	CHF ₂	-6.95	-8.36
B_21		(3-morpholinophenyl)amino	cPr	CHF ₂	-8.00	-7.94
B_22		(1-methyl-1H-imidazol-4-yl)amino	cPr	CHF ₂	-7.41	-7.61
B_23		tetrahydro-2H-pyran-4-carboxamido	cPr	CHF ₂	-6.62	-8.44
B_24		3-methoxypropanamido	cPr	CHF ₂	-6.74	-7.85
B_25		(2-morpholinoethyl)amino	cPr	CHF ₂	-7.10	-8.38
B_26		2-morpholinoethoxy	cPr	CHF ₂	-7.29	-8.77
B_27		2-(tetrahydro-2H-pyran-4-yl)ethoxy	cPr	CHF ₂	-8.21	-9.22
B_28 – B_32						
	Compound	R ₁	-pIC ₅₀ (M)			
B_28		6-(cyclopropylcarbamoyl)-5-methoxypyridin-3-yl		-5.58	-6.81	-7.24
B_29		6-(cyclopropylcarbamoyl)-5-(difluoromethoxy)pyridin-3-yl		-6.06	-6.94	-7.25
B_30		5-methoxy-6-((2,2,2-trifluoroethyl)carbamoyl)pyridin-3-yl		-5.42	-6.62	-6.93
B_31		2-cyclopropyl-8-methoxy-1-oxo-1,2,3,4-tetrahydroisoquinolin-6-yl		-5.79	-7.28	-7.93
B_32 (GLPG3970)		8-methoxy-1-oxo-2-(2,2,2-trifluoroethyl)-1,2,3,4-tetrahydroisoquinolin-6-yl		-6.55	-8.11	-8.42

Table 1. Structures and activities of SIK1, SIK2, and SIK3 inhibitors.

Interaction fingerprint (IFP)

Interaction fingerprints (IFPs) are a computational method used to describe the interactions between a protein and a ligand in a concise, binary format. These fingerprints translate the complex three-dimensional (3D) structure of a protein-ligand complex into a simplified, one-dimensional representation, indicating whether specific interactions occur between the ligand and amino acids in the protein's binding site⁴⁹. By doing so, IFPs provide a quick overview of the interaction patterns present in the complex.

In this work, IFPs were calculated for the docked ligand poses and the amino acid residues in the SIK1, SIK2, and SIK3 active sites. To generate these fingerprints, we used the Interaction Fingerprint panel available in Maestro. This tool builds an interaction matrix by detecting various types of non-covalent interactions, including hydrophobic (H), polar (P), aromatic (Ar), HB acceptors (A) and donors (D), and charged (Ch) groups. An interaction was defined as present when a residue in the PK binding pocket was located within 4.0 Å of the heavy atoms of the ligand. The definitions of the IFPs for HBs are as follows: The maximum H...A distance was 2.5 Å; the minimum donor angle (D-H...A) was 120°; and the minimum acceptor angle (H...A-X) was 90°.

Gaussian accelerated molecular dynamics (GaMD) and correlation analysis

To thoroughly explore the conformational landscape of the SIK1, SIK2, and SIK3 binding sites, MD simulations were employed. These simulations were conducted with **A_22** bound to the active site to ensure its openness and flexibility for subsequent cross-docking studies. The structures of the complexes including **A_22** obtained with docking served as the starting points.

Protein structures were prepared using the Protein Preparation Wizard in Schrödinger LLC, ensuring proper protonation states. Each system was then solvated in a truncated octahedral box filled with TIP3P water molecules, neutralized, and adjusted to a 0.15 M NaCl concentration, ensuring a minimum buffer distance of 12 Å between the protein and the box boundary. NAMD v2.14⁵⁰ and CHARMM36⁵¹ were used as the force field and simulation engine; the parameters for **A_22** were generated using the CHARMM General Force Field

(CGenFF)⁵². Energy minimizations were performed for 30,000 steps to relax steric clashes and optimize the systems. 10 ns equilibration was carried out under isothermal-isobaric (NPT) conditions at 310 K and 1 atm.

Gaussian accelerated MD (GaMD) simulations were performed to enhance conformational sampling⁵³. In the GaMD protocol for each system, the threshold energy added to bias the potential was set to the maximum potential ($E = V_{\max}$)⁵⁴. A total of 10 ns of conventional MD, 50 ns of equilibration, and 300 ns of production simulations were conducted. These simulations were sufficient to capture conformational variability in the binding site due to the enhanced sampling provided by GaMD. Trajectories were analyzed using VMD⁵⁵, extracting key descriptors of structural flexibility in the active site.

To identify distinct conformations within the binding sites, clustering of the MD trajectories was performed using the hierarchical agglomerative (HierAgglo) algorithm in CPPTRAJ⁵⁶, with RMSD-based distance metrics. A cutoff of 5 was applied, and the clustering process was configured to produce ten clusters using the average linkage method. This number ensured a manageable and representative sampling of distinct conformational states across the trajectory, providing structural diversity while minimizing redundancy. The representative frame for each cluster was chosen as the one with the smallest cumulative distance to all other frames within the cluster.

Docking simulations were conducted for each ligand using the parameters specified in Sect. 2.3. The resulting poses were evaluated based on their docking scores, and an *in-house* genetic algorithm (GA) was used to select the pose ensemble best correlated with experimental activity data (expressed as pIC_{50} values). This Python-based algorithm⁵⁷ optimized the correlation by applying genetic operations, including one-point crossover and single-point mutation, with probabilities of 0.6 and 0.1, respectively. Elitism ensured retention of the top 30% of combinations in each generation to preserve high-quality solutions.

This workflow enabled the generation of models for the 44 inhibitors forming complexes with SIK1, SIK2, and SIK3, where the calculated docking energies correlated with the experimentally reported activities. These models exhibit conformational diversity in the binding sites of SIK1, SIK2, and SIK3, as derived from the GaMD simulations and clustering protocol.

Results and discussion

Docking results

The SIK3 structure was used as a template to model the structures of SIK1 and SIK2. SIK1 shares 77.7% sequence identity and 58.0% sequence similarity with SIK3, while SIK2 shares 75.3% sequence identity and 58.4% sequence similarity with SIK3. These values demonstrate a high degree of similarity among the studied PKs, which is expected to correspond to significant structural resemblance. The quality of the models was evaluated using PROCHECK⁵⁸ (Ramachandran plots are provided in the supplementary material, Figure S1).

Docking simulations were conducted to explore how the 44 inhibitors interact with SIK1, SIK2, and SIK3. Supplementary Table S1 provides the docking score energies obtained from these calculations. The findings indicate that the ligands in the series adopt a consistent binding mode (Fig. 2). Following the criteria for obtaining acceptable poses, suitable poses were found for the vast majority of the compounds. However, it was not possible to find poses for the weakly active compound A_18 in any of the three PKs. In SIK1, no poses were found for B_10, B_21, and B_27 either. In SIK2, additional poses could not be found for B_17. Finally, in SIK3, no poses were identified for A_19, B_27, B_29, and B_30. The poor results for compound A_18, considering its *tert*-butyl substituent, were expected. Moreover, A_18 is the least effective compound in the series, with activities above a threshold for all three SIKs. The lack of solutions for other compounds could be attributed to the rigidity of the binding sites.

It can be observed that all the compounds exhibited interactions with the hinge region, characteristic of ATP-competitive PK inhibitors. In all cases, the HB between the N3 of the 1*H*-benzo[d]imidazole (series A) or the N1 of the imidazo[1,2-*a*]pyridine (series B) and the NH of alanine *h3* in the hinge region (A106, A99, and A145 in SIK1, SIK2, and SIK3, respectively) was conserved. Additionally, an HB between the polar groups positioned at the *para* position of the phenyl substituent at the main scaffold and the NH_3^+ of the catalytic lysine (K56, K49, and K95 in SIK1, SIK2, and SIK3, respectively) was also preserved. The R substituents (Table 1) on the six-membered rings of the ligand scaffolds were oriented toward the outer part of the SIK binding sites, near the loops of subdomain V after the hinge region. The orientations obtained are similar to that of compound A_22 in SIK3 in the PDB with code 8OKU¹².

The poses obtained for A_22 were compared with its pose in the crystal structure 8OKU. The RMSD values obtained were 1.00, 2.73, and 0.55 Å for SIK1, SIK2, and SIK3, respectively (Figure S2 in the supplementary material). Although the RMSD value for SIK2 exceeds 2.5 Å, it can be observed that the main scaffold is correctly oriented (Figure S2B), indicating that the obtained pose is appropriate. The RMSD value increases due to differences in the orientations of the side groups. Specifically, the ethylcarbamoyl group changes its orientation without losing the HB with the catalytic lysine, while the 1-(2-hydroxyethyl)-1*H*-pyrazol-4-yl group changes its orientation in a region exposed to the solvent. Based on these observations, the docking result for A_22 in SIK2 serves as an example of a correct orientation obtained through docking, despite not meeting the typical rule of requiring an RMSD value below 2 Å.

The similarity in the orientations of the 44 inhibitors within the three PKs was evaluated using the LigRMSD server⁴⁸. The pose of the ligand A_22 in SIK3 from the 8OKU crystal structure was used as a reference. The results of this evaluation are presented in Table S2 of the supplementary material. Similar orientations between poses are characterized by low RMSD values. Since non-identical ligands were compared, it is necessary to check the %RefM and %MolM values (previously defined) to estimate the proportion of molecules being compared. The strict or flexible mode was used depending on whether the graphs being compared were identical or not. As the compounds in series A share the same scaffold as the reference A_22, the strict mode was more frequently

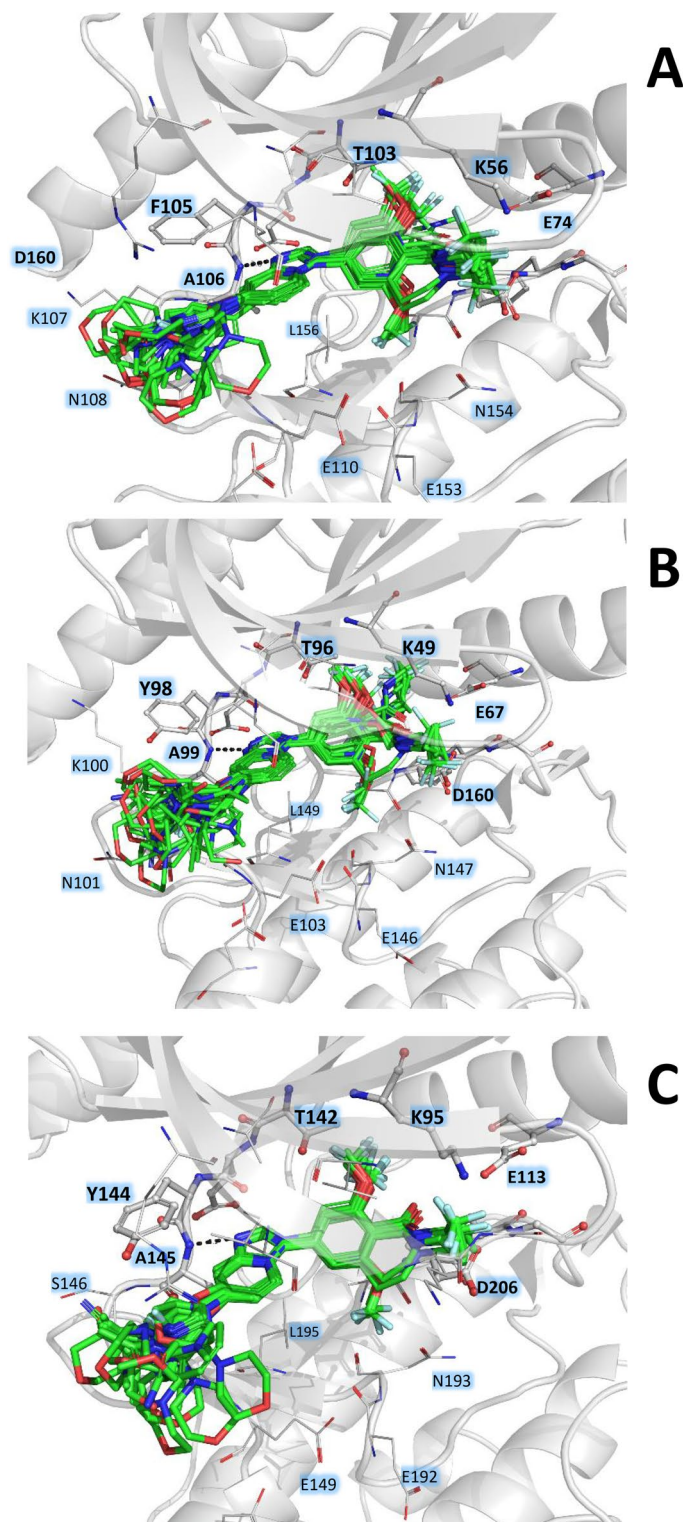


Fig. 2. Docked structures within the SIK1 (A), SIK2 (B), and SIK3 (C) binding sites. Docked ligands are represented by green sticks. Relevant residues at protein subsites are represented by gray sticks. Hydrogens are omitted for clarity.

applied to them. On the other hand, since the compounds in series B (except for **B_10**) have a different distribution of N atoms in the heterocycle compared to **A_22**, the flexible mode was used for them.

All compounds in series A exhibited %RefM or %MolM values above 87%, demonstrating their similarity to the reference compound **A_22**. The RMSD values for these compounds were below 2 Å in SIK1 and SIK3. However, several compounds showed RMSD values above 2 Å in SIK2 (including compound **A_22** itself, as

mentioned earlier). As with the docking of **A_22** in SIK2, these other compounds correctly oriented their main scaffold, forming an HB with the NH of alanine A99 (*h3* in the hinge region). The ethylcarbamoyl groups in compounds **A_15**, **A_20**, and **A_21** changed their orientations without losing the HB with the catalytic lysine. Compound **A_16** exhibited behavior similar to that observed for the docking pose of **A_22** in SIK2, with both side groups oriented differently but maintaining the scaffold correctly aligned.

Regarding the series B compounds, their %RefM or %MolM values ranged from 56.25 to 78.12 using the flexible model, reflecting lower similarity to the reference compound **A_22** but sufficient graph concordance to establish a valid comparison. Compounds **B_31** and **B_32** showed the lowest %RefM and %MolM values (56.25) because both contain substituents derived from the 8-methoxy-1-oxo-1,2,3,4-tetrahydroisoquinolin-6-yl group. LigRMSD identified the common graph between these substituents and the 4-carbamoyl-3-methoxyphenyl group present in **A_22**, also including the heterocycle as the main scaffold. The remaining compounds in series B shared with **A_22** the graph comprising the heterocycle and the 4-carbamoyl-3-methoxyphenyl substituent, with differences in the orientations of the more external substituents. As with series A, the RMSD values for all series B compounds were below 2 Å in SIK1 and SIK3 (in fact, below 1 Å). In SIK2, RMSD values were also low, except for three compounds (**B_10**, **B_11**, and **B_15**). These compounds also correctly oriented their main scaffold, forming the HB in the hinge region, but the (2,2,2-trifluoroethyl)carbamoyl group (analogous to the ethylcarbamoyl group in **A_22**) also changed its orientation without losing the HB with the catalytic lysine.

We examined the structures to investigate why the described differences in poses were observed only in SIK2. It was found that in SIK2, the M71 residue, conserved in the α C-helix of all three SIKs (M78 in SIK1 and M117 in SIK3), oriented its side chain differently in the developed SIK2 model, creating a space that allows for the potential placement of ligand groups. Thus, we confirmed that the differences were not due to the presence of different residues.

The IFPs revealed the recurrence of interactions between the docked ligands and the three PKs. Figure 3A and B show the IFPs corresponding to the studied compounds docked in the SIK1 model. The fundamental interactions extensively documented for ATP-competitive PK inhibitors⁵⁹ can be detected in the IFPs. The IFPs for SIK1 display contacts with the gatekeeper residue T103 and the hinge region residues *h1*, *h2*, and *h3* (E104, F105, and A106, respectively) with occurrences close to 100%. These contacts include the formation of aromatic interactions with F105 (*h2*) and an HB with A106 (*h3*). High occurrence percentages also highlight interactions with the catalytic lysine K56 (forming an HB at 100%), the conserved glutamate E74 from the α C-helix (85%), and the aspartate D167 from the DFG motif (100%). Hydrophobic interactions with residues L33, V41, and A54 at the N-lobe hydrophobic wall appear in the IFPs with occurrence percentages of 90%, 45%, and 100%, respectively. Meanwhile, interactions with residues I87, L156, and A166 at the C-lobe hydrophobic wall occur with 10%, 100%, and 100% frequency, respectively. The last two residues of the HRDLKXXN consensus motif in subdomain VIB, E153 and N154, contribute with 67.5% and 27.5% occurrence, respectively. Additionally, significant contributions to the interactions come from the side chain of R31 (67.5%) in subdomain I and residues K107 (85%) and G109 (95%) in the loop of subdomain V, located after the hinge region.

The IFPs for the studied compounds docked in the SIK2 model are presented in Fig. 3E and F. Contacts with the gatekeeper residue T96, the hinge region residues (E97, Y98, and A99), the catalytic lysine (K49), the conserved glutamate from the α C-helix (E67), and the DFG aspartate (D160) make significant contributions, very similar to what was observed for SIK1. Hydrophobic interactions with residues L26, V34, and A47 at the N-lobe hydrophobic wall appear in the IFPs with occurrence percentages of 100%, 90.5%, and 100%, respectively. Meanwhile, interactions with residues I80, L149, and A159 at the C-lobe hydrophobic wall occur with frequencies of 19%, 100%, and 100%, respectively. The residues from subdomain VIB, E146 and N147, contribute with 42.9% and 69.0% occurrence, respectively. Additionally, residues K100 and G102 in the loop of subdomain V, located after the hinge region, contribute with 71.4% and 100%, respectively.

Finally, the IFPs for the studied compounds docked in the SIK3 structure 8OKU are shown in Fig. 3I and J. Contacts were observed between all compounds and the gatekeeper residue T142, the hinge region residues (E143, Y144, and A145), the catalytic lysine (K95), and the DFG aspartate (D206), very similar to what was observed for SIK1 and SIK2. As a difference, the IFPs do not show contacts with the conserved glutamate from the α C-helix (E113). All the compounds exhibit hydrophobic interactions with residues I72, V80, and A93 at the N-lobe hydrophobic wall. Meanwhile, interactions with residues I126, L195, and A205 at the C-lobe hydrophobic wall occur with frequencies of 12.8%, 100%, and 53.8%, respectively. The residues from subdomain VIB, E192 and N193, contribute with 84.6% and 89.7% occurrence, respectively. Additionally, residues S146 and G148 in the loop of subdomain V, located after the hinge region, contribute with 74.4% and 100%, respectively. The residue R70 in subdomain I plays a significant role (76.9%), similar to the analogous residue R31 in SIK1.

Overall, the IFP results for the three SIKs in rigid models show very subtle differences, primarily in hydrophobic interactions. Very few residues change in the binding sites, which suggests that exploring differences further would benefit from using different receptor conformations in the cross-docking experiments.

Cross-docking results

According to what is observed in the PDB structure with code 8OKU, **A_22** fits a Type I pharmacophore within a DFG-in conformation of the PK. The studied compounds, which are congeneric with **A_22**, adopt similar orientations in the binding sites of SIK1, SIK2, and SIK3 in previous docking experiments. Therefore, they are also classified as Type I inhibitors. An analysis of the substituent positions within the binding sites shows that the studied compounds lack the functional groups required to induce a conformational change of the PKs to the DFG-out state⁵⁹, and thus, during a flexibility exploration, it is expected that the PKs remain in the DFG-in conformation. The exploration of SIK flexibility aims to detect orientation changes in binding site residues to identify new solutions in docking calculations. It is not necessary to explore large-scale conformational changes in the PKs for this purpose.

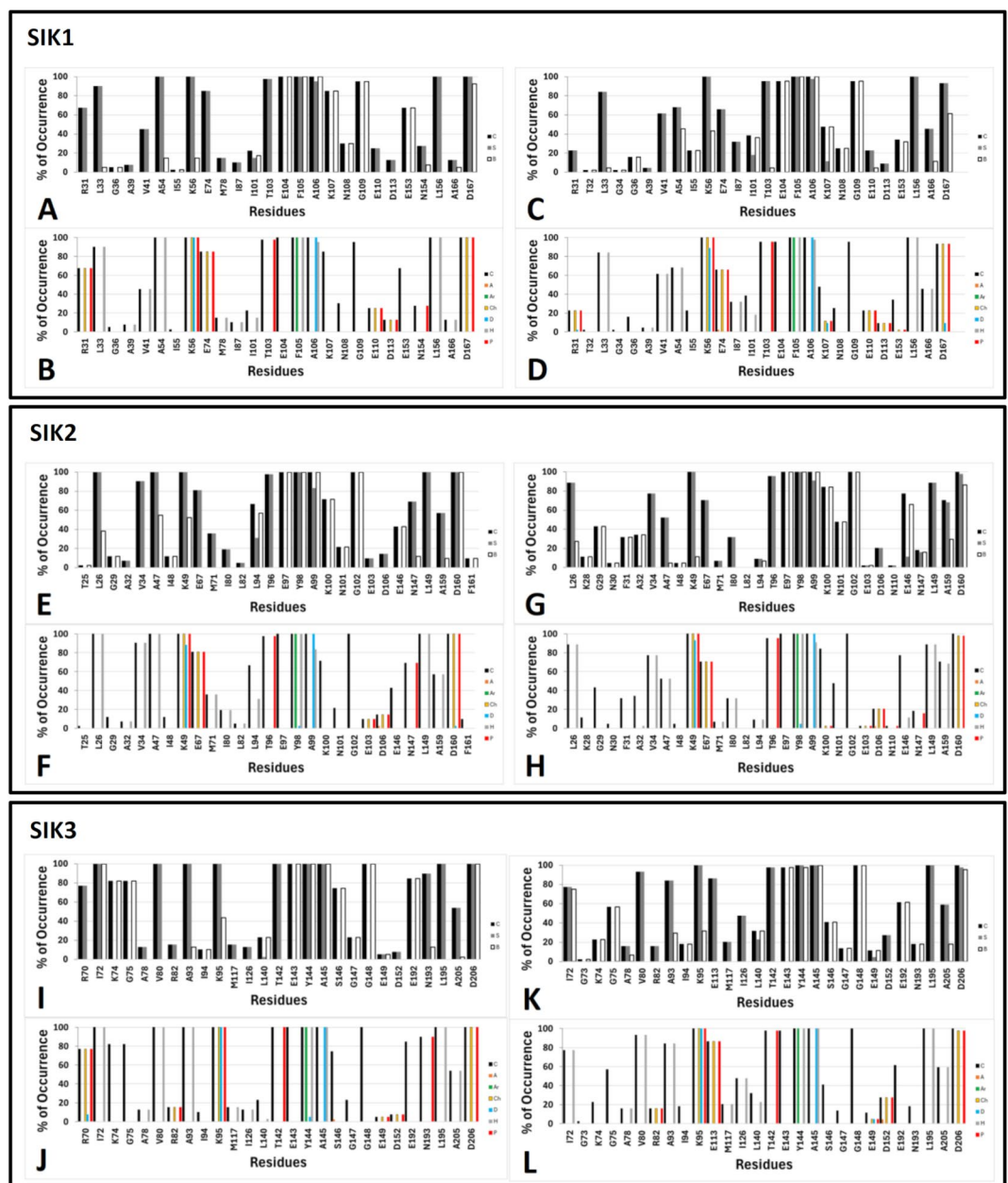


Fig. 3. IFPs illustrating the docking outcomes between the compounds and SIK1, SIK2, and SIK3. (A, B) Interactions between the compounds and residues in the SIK1 model. (C, D) Interactions in the SIK1–ligand complexes obtained through cross-docking, which maximize the correlation with biological activities. (E, F) Interactions between the compounds and residues in the SIK2 model. (G, H) Interactions in the SIK2–ligand complexes obtained through cross-docking, which maximize the correlation with biological activities. (I, J) Interactions between the compounds and residues in the SIK3 crystal structure (PDB ID: 8OKU). (K, L) Interactions in the SIK3–ligand complexes obtained through cross-docking, which maximize the correlation with biological activities. The top panels in each box (A, C, E, G, I, K) display the percentage of occurrences for contacts [C], side-chain interactions [S], and backbone interactions [B]. The bottom panels in each box (B, D, F, H, J, L) show the occurrence percentages of various interaction types, including contacts [C], HB acceptors [A], aromatic interactions [Ar], charged group interactions [Ch], HB donors [D], hydrophobic interactions [H], and polar interactions [P].

The rigid structures of the PKs initially used in the docking experiments may represent limited depictions of reality, as they do not account for the intrinsic flexibility of the receptors. As a more realistic alternative, various conformations of SIK1, SIK2, and SIK3 were obtained through GaMD simulations, following the previously described protocol. These protein model variants allowed for the exploration of a broader range of inhibitor conformations within the binding sites. Simulations were performed on solvated structures of SIK1, SIK2, and SIK3 in complex with A_22 to maintain the binding sites open. The trajectories displayed stable behavior during

the production stages (RMSD plots of the backbone atoms over time are shown in the supplementary material, Figure S3).

Using clustering, as described previously, ten conformations were obtained for each SIK, representing different orientations of the residues within the binding sites that were sampled during the GaMD simulation trajectories. These conformations of SIK1, SIK2, and SIK3 are referred to as Sik1_c0-c9, Sik2_c0-c9, and Sik3_c0-c9, respectively, throughout this manuscript. Cross-docking calculations were performed, where the 44 compounds were docked into all conformations. This process yielded up to ten different poses for each ligand in SIK1, SIK2, and SIK3, along with their respective scoring energy values. It was essential to ensure that the poses obtained were not entirely different from the pose of **A_22** in 8OKU, as this served as our reference for selecting high-quality poses. It is well-documented in the literature that ATP-competitive PK inhibitors follow a set of interactions that mimic those originally formed by ATP, and this knowledge was considered during docking calculations^{59,60}. Pose evaluation was carried out using LigRMSD⁴⁸ and visual inspection. Subsequently, a representative complex for each SIK-ligand pair was selected using a custom Python script developed *in-house*⁵⁷. This script employs a GA to identify the set of poses that optimally correlates the calculated scoring values with the experimental activities. As a result, the script provided the sets of cross-docking complexes for SIK1, SIK2, and SIK3 with the 44 studied compounds that best describe the differences in activity within the datasets. The calculated energies associated with these complexes are provided in the final columns of Table S1 in the supplementary material.

To analyze the obtained correlations, Fig. 4 presents plots of docking energy values against logarithmic experimental activities ($-pIC_{50}$) when using a single structure and when using the structures resulting from the GA-based selection. When using a single structure, the correlations were low for SIK1, SIK2, and SIK3, with R^2 values of 0.378, 0.054, and 0.040, respectively (Figs. 4A–C). In these cases, the docking calculated scoring energy values do not show a direct correlation with the observed biological activities. This discrepancy is a known limitation of docking algorithms, as scoring methods often simplify the complex interactions between ligands and receptors, omitting key factors such as receptor flexibility, solvent effects, and thermodynamic contributions associated with entropy^{61–63}. Additionally, these methods are generally designed to prioritize the geometric fit of the ligand within the binding site rather than accurately predicting binding affinity. To address limitations related to protein flexibility, strategies have been developed to consider receptor adaptability during binding⁶⁴. These approaches better capture the complexity of biological systems and can provide results more consistent with experimental observations.

When the structures selected from the GaMD simulation were used for cross-docking experiments, the correlations improved considerably, as shown in Figs. 4D–F. For SIK1, a correlation of $R^2 = 0.821$ was achieved when including all ligands, while for SIK2 and SIK3, correlations with R^2 values of 0.646 and 0.620, respectively, were obtained after excluding the least active compound, **A_18**. As mentioned previously, no docking solutions were found for this compound when using a single rigid structure; **A_18** has a *tert*-butyl substituent that could not fit within the rigid active sites of the three SIKs. When additional conformations were incorporated, solutions for **A_18** were obtained for SIK1, SIK2, and SIK3, but only in SIK1 did the conformation contribute positively to the correlation. In contrast, the complexes formed by **A_18** with SIK2 and SIK3 behaved as outliers in the correlations established for these two enzymes. Experimentally, the activities of **A_18** against the three SIKs did not yield precise results, making its behavior in our models unsurprising.

The flexibility in the binding sites allowed solutions to be found for all compounds (except **A_18**) across the three SIKs in cross-docking experiments, which was not achieved when docking calculations were performed on rigid structures. The improved correlations for the studied compounds as inhibitors of SIK1, SIK2, and SIK3 suggest that considering the flexibility of the SIKs is essential to describe the differential activities of the compounds accurately. From the ten conformations obtained for each SIK, our script identified six conformations of SIK1 (Sik1_c1, Sik1_c5, Sik1_c6, Sik1_c7, Sik1_c8, and Sik1_c9), five conformations of SIK2 (Sik2_c1, Sik2_c3, Sik2_c6, Sik2_c8, and Sik2_c9), and four conformations of SIK3 (Sik3_c5, Sik3_c6, Sik3_c8, and Sik3_c9) as contributors to the models that described the optimal correlations between energies and activities. These conformations, along with the associated compounds for each of the three models, are reported in Table 2. Additionally, the 3D structures of the inhibitors in MOL2 format, in the conformations of SIK1, SIK2, and SIK3 in PDB format, are available as supplementary material in the file *Structures.zip*.

The fact that selecting multiple conformations of the SIKs allowed to find models where docking energies correlated with inhibitory activities is due to the presence of different orientations of residues in the binding sites. These orientations, captured during the GaMD simulations, generated new shapes and distributions of chemical groups, enabling the identification of new poses in the cross-docking calculations. Next, we analyze which residues underwent the most significant conformational changes in SIK1, SIK2, and SIK3.

In the first instance, we checked the residues of SIK1, SIK2, and SIK3 that appear in the IFPs derived from these cross-docking calculations in different conformations (Fig. 3, panels C, D, G, H, K, L). As expected, the IFPs are similar to those we previously analyzed for the three PKs. This supports the fact that the obtained poses maintain the expected interactions for ATP-competitive PK inhibitors⁵⁹. The main differences between the IFPs for the three SIKs were due to certain residues, which, despite having contacts with only a few ligands, showed different interaction patterns. For example, the conserved methionine in the α C-helix of all three SIKs showed fewer ligand contacts when site flexibility was considered, compared to those observed in the rigid models. Although flexibility allows for the presence of multiple conformations, this methionine M117 in SIK3 interacted with only 20% of the ligands (Figs. 3K, L), while M78 in SIK1 showed no contacts (Figs. 3C, D), and M71 in SIK2 interacted with only 8% of the compounds (Figs. 3G, H). Given these low interaction percentages, although some differences are observed, it would be difficult to attribute a role in SIK selectivity to this methionine, as it directly interacts with only a few compounds.

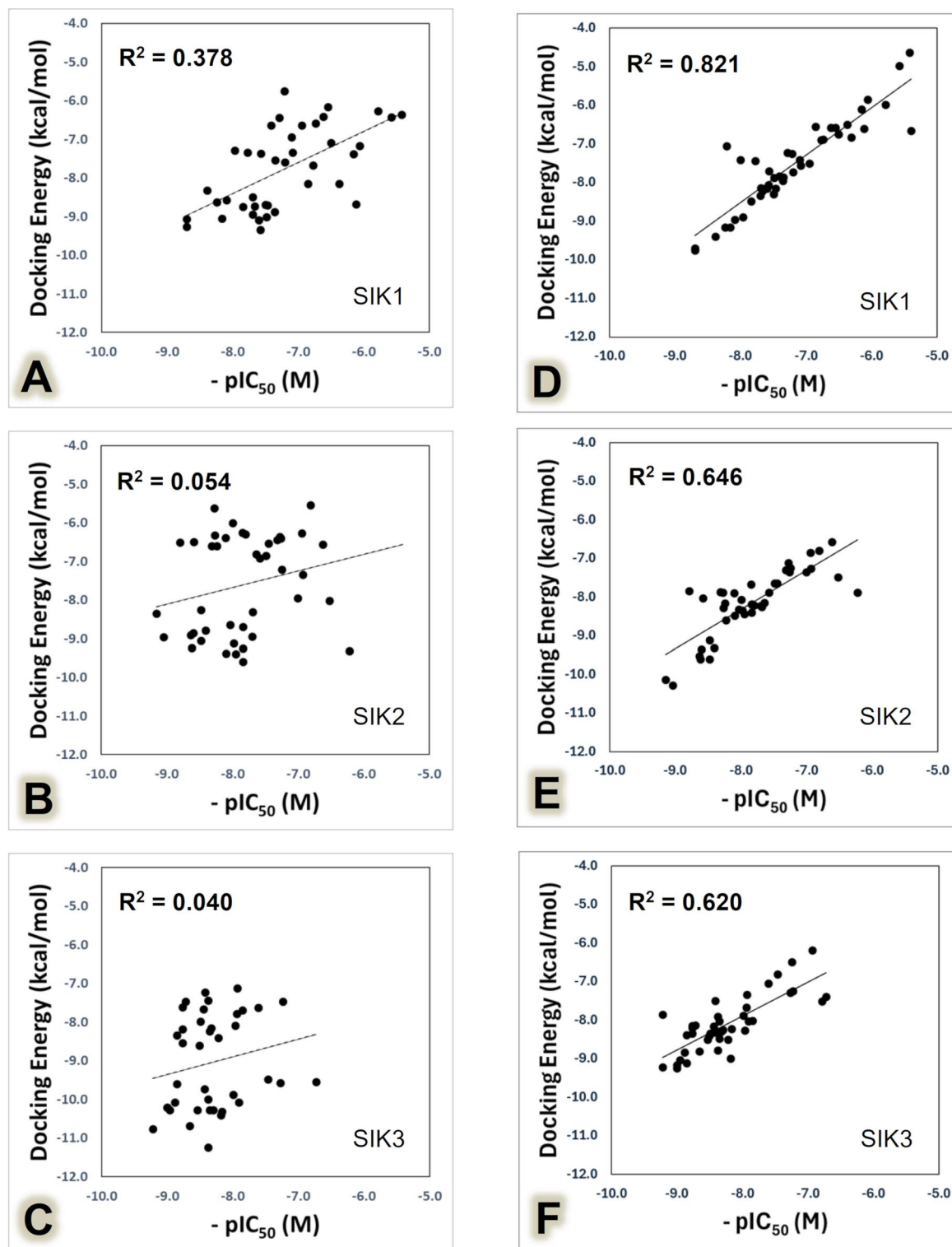


Fig. 4. Regression plots of docking scores versus experimental activities ($-pIC_{50}$) for docking calculations in a single PDB structure (left panels) and cross-docking performed on selected protein conformations (right panels). (A, D) SIK1; (B, E) SIK2; (C, F) SIK3.

We reviewed the root mean square fluctuations (RMSF) for all residues with an occurrence percentage above 20% in the IFPs to identify those with significant conformational differences among the SIK1, SIK2, and SIK3 structures used in the cross-docking calculations (Figure S4 in the Supplementary Material). It can be observed that the residues showing the greatest differences among the structures are not those typically identified as key features of PKs—such as the catalytic lysine, the gatekeeper, or the hinge region residues. Some differences are

SIK1 Conformation	Ligands	SIK2 Conformation	Ligands	SIK3 Conformation	Ligands
Sik1_c1	A_16, A_17, A_20, B_21, B_27, B_32	Sik2_c1	A_17, A_20, B_23, B_28, B_29, B_30	Sik3_c5	A_10, A_16, A_17, A_19, A_20, A_24, A_27, A_28, B_29, B_30
Sik1_c5	A_12, A_27, B_11, B_13, B_23	Sik2_c3	A_12, A_16, A_24, A_27, B_11, B_15, B_24, B_25, B_31	Sik3_c6	A_12, A_15, A_23, A_26, B_22
Sik1_c6	A_11, A_22, A_23, A_24, A_26, B_15, B_31	Sik2_c6	A_11, A_15, A_21, A_26, B_10	Sik3_c8	B_11, B_12, B_13, B_14, B_15, B_16, B_17, B_18, B_19, B_20, B_21, B_23, B_24, B_25, B_26, B_27, B_28, B_31, B_32
Sik1_c7	A_10, A_28, B_12, B_14, B_16, B_17, B_18, B_19, B_20, B_22, B_24, B_25, B_26	Sik2_c8	A_08, A_09, A_13, A_14, A_19, A_22, A_23, A_25	Sik3_c9	A_08, A_09, A_11, A_13, A_14, A_21, A_22, A_25, B_10
Sik1_c8	A_13, A_14, A_15, A_21, A_25, B_29	Sik2_c9	A_10, A_28, B_12, B_13, B_14, B_16, B_17, B_18, B_19, B_20, B_21, B_22, B_26, B_27, B_32		
Sik1_c9	A_08, A_09, A_18, A_19, B_10, B_28, B_30				

Table 2. Definition of protein-ligand pairs obtained through cross-docking for SIK1, SIK2, and SIK3 forming complexes with the studied inhibitors.

observed in the residues exhibiting the most variable orientations in SIK1, SIK2, and SIK3, which we further analyze by constructing RMSD matrices.

As mentioned earlier, six SIK1 structures were included in the model that showed the highest correlation with the experimental pIC_{50} values. The RMSD value matrices, comparing the residues in the ATP-binding site, are provided in the supplementary material (Figure S5), identifying the distinctive features of PK binding sites. The residues with the highest RMSD values are highlighted in Fig. 5, along with a schematic representation of the SIK1 binding site. Below, we discuss some of the residues that exhibited the most significant conformational differences in the SIK1 site. The most notable conformational changes are observed in residues L33 and V41 of the N-lobe hydrophobic wall, in residues K107, N108, G109, and E110 of subdomain V after the hinge region, in residue E153 of the HRDLKXXN consensus motif in subdomain VIB, and in R31 of subdomain I, before the glycine-rich loop. The changes in charged polar residues, such as the catalytic lysine K56, the conserved glutamate in the α C-helix E74, and the DFG aspartate D167, are less pronounced but highly relevant, as the relocation of these charged groups influences the docking solutions obtained. Overall, Fig. 5 illustrates a set of residues that shift their positions to varying degrees in SIK1, altering the shape and charge distribution of the active sites. This allowed us to account for the flexibility of the binding site in our approach.

In the case of SIK2, five structures were included in the model that showed the highest correlation with the experimental pIC_{50} values. The RMSD value matrices, comparing the residues in the ATP-binding site, are provided in Figure S6 of the supplementary material, highlighting the distinctive features of PK binding sites. The residues with the highest RMSD values are represented in Fig. 6, along with a schematic representation of the SIK2 binding site. Residue E146 of the HRDLKXXN consensus motif in subdomain VIB, as well as residues G29, F31, and A32 of the glycine-rich loop, exhibited the most significant conformational changes in the SIK2 site. In contrast, the charged groups in the catalytic lysine K49, the conserved glutamate in the α C-helix E67, and the DFG aspartate D160 showed less conformational variation in SIK2 compared to SIK1.

Finally, in the case of SIK3, four structures were included in the model that showed the highest correlation with the experimental pIC_{50} values. The RMSD value matrices, comparing the residues in the ATP-binding site, are provided in Figure S7 of the supplementary material, highlighting the distinctive features of PK binding sites. The residues with the highest RMSD values are represented in Fig. 7, along with a schematic representation of the SIK3 binding site. The most significant conformational changes are observed in residue D152, located in the small helix of subdomain V after the hinge region, as well as in residues K74 and G75 of the glycine-rich loop. Minor changes are detected in the catalytic lysine K95 and the conserved glutamate in the α C-helix E113, whereas greater conformational variations are observed in the DFG aspartate D206.

In general, the differences in the orientation of residues in the binding sites of SIK1, SIK2, and SIK3, whether more pronounced or subtle, contributed to the generation of distinct binding site conformations. This allowed for the identification of different inhibitor poses, each assigned different interaction energy values through docking. Therefore, these differences were crucial in developing the correlated models presented in this study. When comparing the three analyzed PKs, it is evident that SIK1 exhibited the most pronounced conformational changes, which may have contributed to achieving a higher correlation for its inhibitors. Nevertheless, the correlations obtained for SIK2 and SIK3 were also satisfactory.

A useful analysis is to examine whether certain conformations of SIK1, SIK2, and SIK3 are more prone to binding active compounds, while others show a higher affinity for inactive compounds. If planning to conduct a virtual screening, it would be preferable to select those PK conformations that exhibit affinity for active compounds over those that do not. This evaluation can be performed using Table 2. For SIK1, the Sik1_c1 conformation bound to five of the most active inhibitors, whereas Sik1_c9 consistently associated with less active inhibitors. In the case of SIK2, the Sik2_c9 conformation bound to ten of the most active inhibitors (including the three most active overall), while Sik2_c8 was associated with least active inhibitors. Finally, for SIK3, we observed that the most active compounds only bound to Sik3_c5 and Sik3_c8, whereas Sik3_c9 bound

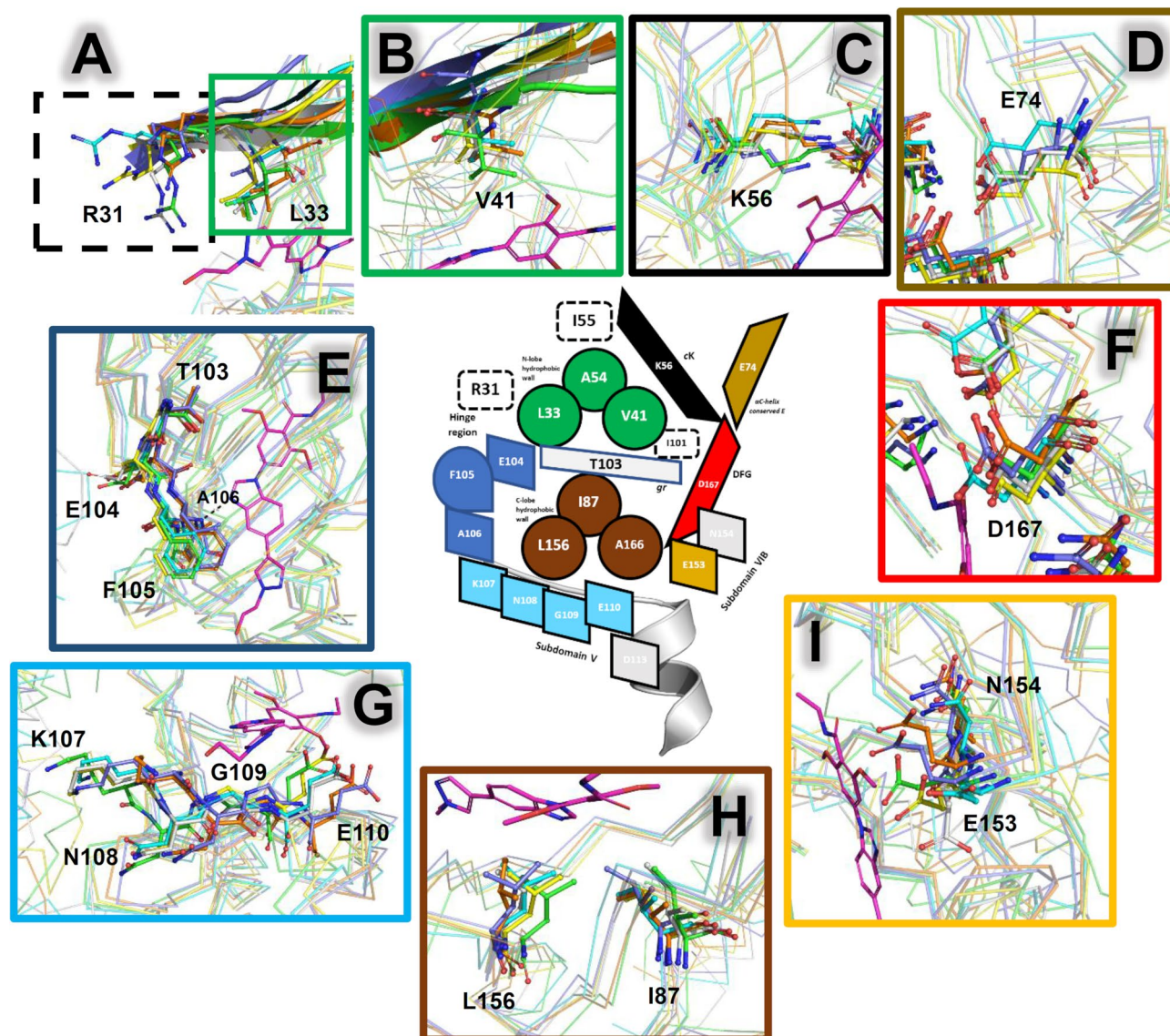


Fig. 5. Schematic representation of the ATP-binding site for SIK1. Residues with IFP contributions above 20% are colored as indicated, and their structures are represented as sticks in panels (A–I). Black, ochre, and red trapezoids represent the catalytic lysine (K56), conserved glutamate (E74), and DFG aspartate (D167), respectively; their structures are shown in panels C, D, and F. The gatekeeper residue (T103) is represented with a white rhombus, while hinge region residues (E104, F105, A106) are represented with blue shapes; their structures are in panel E. Residues following the hinge region (K107, N108, G109, E110) are represented with cyan rhombuses; their structures are shown in panel G. The penultimate residue in subdomain VIB (E153) is represented with an orange rhombus; its structure is shown in panel I. Green and brown circles denote the N-lobe and C-lobe hydrophobic wall residues (L33/V41/A54 and I87/L156/A166), respectively; their structures are shown in panels A, B, and H. Other relevant residues (R31, I55, I101) are enclosed in dashed-line boxes; the structures of R31 are displayed in panel A. The structures in panels (A–I) correspond to the conformations of the residues in the schematic representation in SIK1 structures Sik1_c1 (gray), Sik1_c5 (yellow), Sik1_c6 (orange), Sik1_c7 (cyan), Sik1_c8 (green), and Sik1_c9 (violet). Panel borders match the colors of the schematic representation. The compound A_22 is shown as purple sticks for reference in all panels.

to low-activity compounds. No other notable trends were observed, so we can only suggest that the Sik2_c9, Sik3_c5, and Sik3_c8 conformations appear particularly suitable for identifying active inhibitors of the studied PKs. In contrast, Sik1_c9, Sik2_c8, and Sik3_c9 seem less suitable for identifying new active inhibitors. Since the remaining conformations do not exhibit a clear negative trend, they could also be used to identify new active compounds, introducing a conformational flexibility that should be useful for this type of theoretical-experimental approach.

In a classical docking protocol applied to the modeling of congeneric series of enzyme inhibitors, a rigid protein model is typically used. This approach often leads to good predictions of ligand orientations but fails to

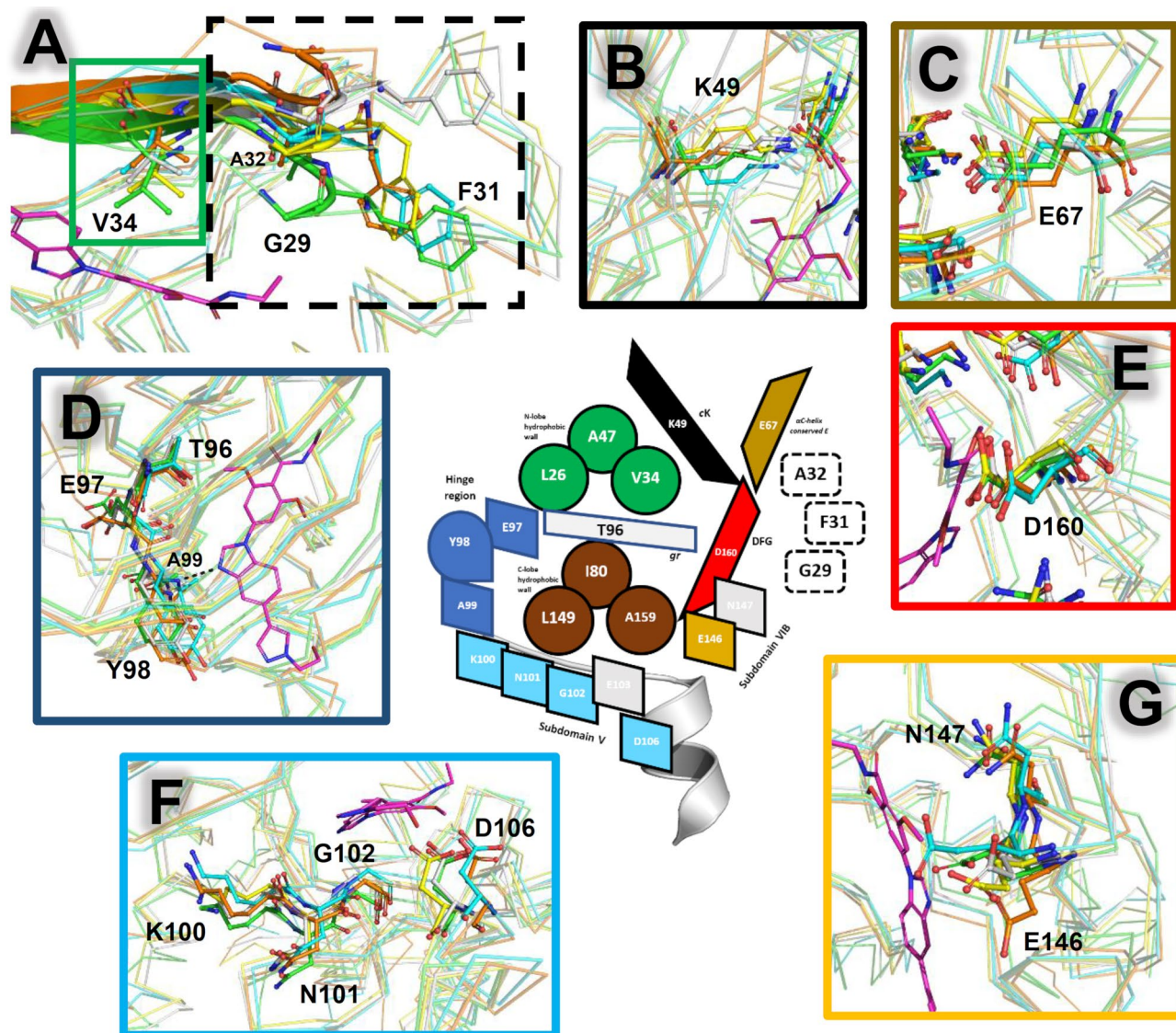


Fig. 6. Schematic representation of the ATP-binding site for SIK2. Residues with IFP contributions above 20% are colored as indicated, and their structures are represented as sticks in panels (A–G). Black, ochre, and red trapezoids represent the catalytic lysine (K49), conserved glutamate (E67), and DFG aspartate (D160), respectively; their structures are shown in panels B, C, and E. The gatekeeper residue (T96) is represented with a white rhombus, while hinge region residues (E97, Y98, A99) are represented with blue shapes; their structures are in panel D. Residues following the hinge region (K100, N101, G102, D106) are represented with cyan rhombuses; their structures are shown in panel F. The penultimate residue in subdomain VIB (E146) is represented with an orange rhombus; its structure is shown in panel G. Green and brown circles denote the N-lobe and C-lobe hydrophobic wall residues (L26/V34/A47 and I80/L149/A159), respectively; the structures of V34 are shown in panel A. Other relevant residues (G29, F31, A32) are enclosed in dashed-line boxes; their structures are in panel A. The structures in panels (A–G) correspond to the conformations of the residues in the schematic representation in SIK2 structures Sik2_c1 (gray), Sik2_c3 (yellow), Sik2_c6 (orange), Sik2_c8 (cyan), and Sik2_c9 (green). Panel borders match the colors of the schematic representation. The compound **A_22** is shown as purple sticks for reference in all panels.

accurately describe differences in binding affinities. In our protocol, different conformations of the SIKs were selected to perform cross-docking calculations. By considering the experimental activity values, we selected the protein-ligand complexes whose docking energy scores correlated best with the inhibitory activities against SIK1, SIK2, and SIK3. The poses obtained are as reasonable as those generated in rigid docking experiments (as demonstrated through the IFP analyses and LigRMSD calculations), allowing us to state that our protocol provides a more realistic description by accounting for protein flexibility.

Classical docking cannot capture important rearrangements in the binding site that may occur when different ligands bind. Our protocol identifies the residues involved in such conformational changes; however, it is important to acknowledge certain limitations of our models. Since our protocol is still based on docking

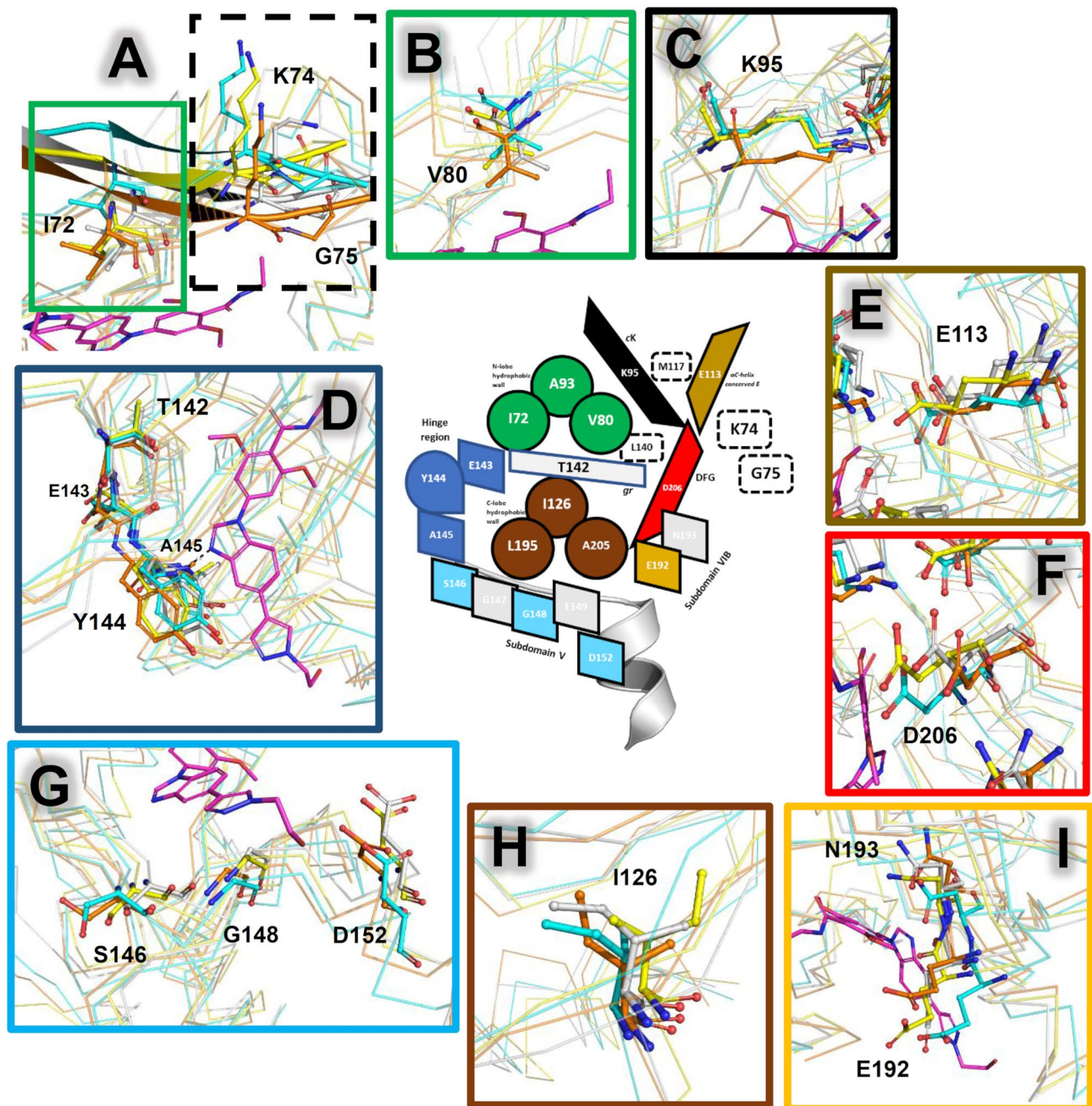


Fig. 7. Schematic representation of the ATP-binding site for SIK3. Residues with IFP contributions above 20% are colored as indicated, and their structures are represented as sticks in panels (A–I). Black, ochre, and red trapezoids represent the catalytic lysine (K95), conserved glutamate (E113), and DFG aspartate (D206), respectively; their structures are shown in panels C, E, and F. The gatekeeper residue (T142) is represented with a white rhombus, while hinge region residues (E143, Y144, A145) are represented with blue shapes; their structures are in panel D. Residues following the hinge region (S146, G148, D152) are represented with cyan rhombuses; their structures are shown in panel G. The penultimate residue in subdomain VIB (E192) is represented with an orange rhombus; its structure is shown in panel I. Green and brown circles denote the N-lobe and C-lobe hydrophobic wall residues (I72/V80/A93 and I126/L195/A205), respectively; their structures are shown in panels A, B, and H. Other relevant residues (K74, G75, M117, and L140) are enclosed in dashed-line boxes; the structures of K74 and G75 are displayed in panel A. The structures in panels (A–I) correspond to the conformations of the residues in the schematic representation in SIK3 structures Sik3_c5 (gray), Sik3_c6 (yellow), Sik3_c8 (orange), and Sik3_c9 (cyan). Panel borders match the colors of the schematic representation. The compound A_22 is shown as purple sticks for reference in all panels.

calculations, the limitations of scoring functions are maintained (binding energies are estimated in a highly simplified manner, and real entropic contributions are not considered). Moreover, our approach relies on the existence of a single experimental protein-ligand complex as a reference (PDB ID: 8OKU). The models for SIK1 and SIK2 were constructed based on the conformation of SIK3 in that reference structure, and suitable poses were selected by comparison to the binding mode of A_22. Therefore, the entire modeling set remains conditioned by this initial choice. These limitations are also inherent to a rigid docking protocol, with the difference that, in rigid docking, the protein conformation is completely fixed and cannot accommodate ligand-induced adjustments.

Conclusion

Recent experimental studies have reported a set of 44 compounds that selectively inhibit the PKs SIK1, SIK2, and SIK3. At the computational level, we aimed to describe these results through molecular models of the complexes, while respecting the available information in the PDB and the knowledge generated on ATP-competitive PK inhibitors. This knowledge is well-established regarding the role of key residues such as those in the hinge region, the catalytic lysine, the DFG motif, the gatekeeper residue, among others. Differences in these residues help guide the design of selective PK inhibitors; however, in SIK1, SIK2, and SIK3, these differences are minimal, as these PKs are structurally closely related. Their ATP-binding sites are nearly identical, making it particularly challenging to develop models that explain selectivity.

Since selectivity information is inherently contained in the IC_{50} values reported for SIK1, SIK2, and SIK3, the construction of structural PK-inhibitor models that also describe activity differences against each PK provides valuable structural insights into this phenomenon. Our objective was to achieve appropriate correlations between the energy values obtained through docking and the pIC_{50} values (derived from the reported IC_{50} values), which we accomplished by considering the flexibility of the three PK structures.

From a structural perspective, the correlated models group PK-ligand complexes in which flexibility was introduced into SIK1, SIK2, and SIK3. The ligand orientations were appropriate, as the main scaffolds maintained orientations very similar to that of the reference compound A_22 in the crystal structure of SIK3 (PDB code 8OKU). The inclusion of flexibility in all three PKs was essential for achieving correlations between docking energies and pIC_{50} values, outperforming the approach that used a single conformation of the PKs. This result is not unexpected, but in this study, it is validated using a relatively simple computational protocol.

The correlations obtained suggest that our models can differentiate between active and inactive inhibitors of SIK1, SIK2, and SIK3. Moreover, our computational protocol enabled the identification of subtle structural differences among the SIKs, which could be leveraged to design inhibitors that specifically target the active regions of one PK without affecting the others. Therefore, the results of this study could help accelerate the drug discovery process by guiding virtual screening experiments to optimize candidate molecules before synthesis and experimental evaluation.

Data availability

The most important data generated or analyzed during this study are included in this published article and its supplementary information files. Data related to intermediate calculations is available from the corresponding author upon reasonable request.

Received: 18 March 2025; Accepted: 21 May 2025

Published online: 29 May 2025

References

- Wein, M. N., Foretz, M., Fisher, D. E., Xavier, R. J. & Kronenberg, H. M. Salt-Inducible kinases: physiology, regulation by cAMP, and therapeutic potential. *Trends Endocrinol. Metab.* **29**, 723–735 (2018).
- Katoh, Y. et al. Salt-inducible kinase (SIK) isoforms: their involvement in steroidogenesis and adipogenesis. *Mol. Cell. Endocrinol.* **217**, 109–112 (2004).
- Sakamoto, K., Bultot, L. & Göransson, O. The Salt-Inducible kinases: emerging metabolic regulators. *Trends Endocrinol. Metab.* **29**, 827–840 (2018).
- Nefla, M., Darling, N. J., van Gijssel Bonnello, M., Cohen, P. & Arthur, J. S. C. Salt inducible kinases 2 and 3 are required for thymic T cell development. *Sci. Rep.* **11**, 21550 (2021).
- Jagannath, A. et al. The multiple roles of salt-inducible kinases in regulating physiology. *Physiol. Rev.* **103**, 2231–2269 (2023).
- Amara, S. et al. Critical role of SIK3 in mediating high salt and IL-17 synergy leading to breast cancer cell proliferation. *PLoS One.* **12**, e0180097 (2017).
- Feng, S. et al. Roles of salt-inducible kinases in cancer (Review). *Int. J. Oncol.* **63**, 118 (2023).
- Lombardi, M. S., Gilliéron, C., Dietrich, D. & Gabay, C. SIK Inhibition in human myeloid cells modulates TLR and IL-1R signaling and induces an anti-inflammatory phenotype. *J. Leukoc. Biol.* **99**, 711–721 (2016).
- Zhou, J. et al. A novel compound ARN-3236 inhibits Salt-Inducible kinase 2 and sensitizes ovarian Cancer cell lines and xenografts to Paclitaxel. *Clin. Cancer Res.* **23**, 1945–1954 (2017).
- Tesch, R. et al. Structure-Based design of selective Salt-Inducible kinase inhibitors. *J. Med. Chem.* **64**, 8142–8160 (2021).
- Peixoto, C. et al. Discovery of clinical candidate GLPG3970: A potent and selective dual SIK2/SIK3 inhibitor for the treatment of autoimmune and inflammatory diseases. *J. Med. Chem.* **67**, 5233–5258 (2024).
- Temal-Laib, T. et al. Optimization of selectivity and Pharmacokinetic properties of Salt-Inducible kinase inhibitors that led to the discovery of Pan-SIK inhibitor GLPG3312. *J. Med. Chem.* **67**, 380–401 (2024).
- McMillan, L. et al. P128 Salt-Inducible kinase 2 is a promising therapeutic target in patients with ulcerative colitis. *J. Crohn's Colitis.* **18**, i422 (2024).
- Cheng, H. et al. SIK1 couples LKB1 to p53-dependent Anoikis and suppresses metastasis. *Sci. Signal.* **2**, ra35 (2009).
- Montenegro, R. C. et al. Identification of molecular targets for the targeted treatment of gastric cancer using dasatinib. *Oncotarget* **11**, 535–549 (2020).
- Zhao, J. et al. SIK2 enhances synthesis of fatty acid and cholesterol in ovarian cancer cells and tumor growth through PI3K/Akt signaling pathway. *Cell. Death Dis.* **11**, 25 (2020).

17. Nagel, S. et al. Amplification at 11q23 targets protein kinase SIK2 in diffuse large B-cell lymphoma. *Leuk. Lymphoma*. **51**, 881–891 (2010).
18. Tarumoto, Y. et al. Salt-inducible kinase inhibition suppresses acute myeloid leukemia progression in vivo. *Blood* **135**, 56–70 (2020).
19. Darling, N. J., Arthur, J. S. C. & Cohen, P. Salt-inducible kinases are required for the IL-33-dependent secretion of cytokines and chemokines in mast cells. *J. Biol. Chem.* **296**, 100428 (2021).
20. Bertorello, A. M. et al. Increased arterial blood pressure and vascular remodeling in mice lacking salt-inducible kinase 1 (SIK1). *Circ. Res.* **116**, 642–652 (2015).
21. Clark, K. et al. Phosphorylation of CRTC3 by the salt-inducible kinases controls the interconversion of classically activated and regulatory macrophages. *Proc. Natl. Acad. Sci. U S A.* **109**, 16986–16991 (2012).
22. Sundberg, T. B. et al. Development of chemical probes for investigation of Salt-Inducible kinase function in vivo. *ACS Chem. Biol.* **11**, 2105–2111 (2016).
23. Ozanne, J., Prescott, A. R. & Clark, K. The clinically approved drugs dasatinib and bosutinib induce anti-inflammatory macrophages by inhibiting the salt-inducible kinases. *Biochem. J.* **465**, 271–279 (2015).
24. Öster, L. et al. The structures of salt-inducible kinase 3 in complex with inhibitors reveal determinants for binding and selectivity. *J. Biol. Chem.* **300**, 107201 (2024).
25. Xiao, Z., Varma, S., Xiao, Y. D. & Tropsha, A. Modeling of p38 mitogen-activated protein kinase inhibitors using the catalyst hypogen and k-nearest neighbor QSAR methods. *J. Mol. Graph Model.* **23**, 129–138 (2004).
26. Kunick, C. et al. Evaluation and comparison of 3D-QSAR CoMSIA models for CDK1, CDK5, and GSK-3 Inhibition by Paullones. *J. Med. Chem.* **47**, 22–36 (2004).
27. Romeiro, N. C., Albuquerque, M. G., de Alencastro, R. B., Ravi, M. & Hopfinger, A. J. Construction of 4D-QSAR models for use in the design of novel p38-MAPK inhibitors. *J. Comput. Aided Mol. Des.* **19**, 385–400 (2005).
28. González, M. et al. 2D autocorrelation modelling of the inhibitory activity of Cytokinin-Derived Cyclin-Dependent kinase inhibitors. *Bull. Math. Biol.* **68**, 735–751 (2006).
29. Sharma, P. & Ghoshal, N. Exploration of a binding mode of benzothiazol-2-yl acetonitrile pyrimidine core based derivatives as potent c-Jun N-terminal kinase-3 inhibitors and 3D-QSAR analyses. *J. Chem. Inf. Model.* **46**, 1763–1774 (2006).
30. Kulkarni, R. G., Srivani, P., Achaiah, G. & Sastry, G. N. Strategies to design Pyrazolyl Urea derivatives for p38 kinase Inhibition: a molecular modeling study. *J. Comput. Aided Mol. Des.* **21**, 155–166 (2007).
31. Caballero, J., Fernández, M., Saavedra, M. & González-Nilo, F. D. 2D autocorrelation, CoMFA, and CoMSIA modeling of protein tyrosine kinases' Inhibition by substituted pyrido[2,3-d]pyrimidine derivatives. *Bioorg. Med. Chem.* **16**, 810–821 (2008).
32. Caballero, J., Fernández, M. & González-Nilo, F. D. Structural requirements of pyrido[2,3-d]pyrimidin-7-one as CDK4/D inhibitors: 2D autocorrelation, CoMFA and CoMSIA analyses. *Bioorg. Med. Chem.* **16**, 6103–6115 (2008).
33. Du, J., Lei, B., Qin, J., Liu, H. & Yao, X. Molecular modeling studies of vascular endothelial growth factor receptor tyrosine kinase inhibitors using QSAR and Docking. *J. Mol. Graph Model.* **27**, 642–654 (2009).
34. Lyne, P. D., Lamb, M. L. & Saeh, J. C. Accurate prediction of the relative potencies of members of a series of kinase inhibitors using molecular Docking and MM-GBSA scoring. *J. Med. Chem.* **49**, 4805–4808 (2006).
35. Lee, K. et al. Pharmacophore modeling and virtual screening studies for new VEGFR-2 kinase inhibitors. *Eur. J. Med. Chem.* **45**, 5420–5427 (2010).
36. Alzate-Morales, J. H., Vergara-Jaque, A. & Caballero, J. Computational study on the interaction of N1 substituted pyrazole derivatives with B-Raf kinase: an unusual water wire Hydrogen-Bond network and novel interactions at the entrance of the active site. *J. Chem. Inf. Model.* **50**, 1101–1112 (2010).
37. Lv, M. et al. Structural insights into flavones as protein kinase CK2 inhibitors derived from a combined computational study. *RSC Adv.* **5**, 462–476 (2014).
38. Lv, M. et al. Computational studies on the binding mechanism between Triazolone inhibitors and Chk1 by molecular Docking and molecular dynamics. *Mol. Biosyst.* **11**, 275–286 (2015).
39. Singh, N., Tiwari, S., Srivastava, K. K. & Siddiqi, M. I. Identification of novel inhibitors of Mycobacterium tuberculosis PknG using pharmacophore based virtual screening, docking, molecular dynamics simulation, and their biological evaluation. *J. Chem. Inf. Model.* **55**, 1120–1129 (2015).
40. Shi, M. et al. Dasatinib-SIK2 binding elucidated by homology modeling, molecular docking, and dynamics simulations. *ACS Omega*. **6**, 11025–11038 (2021).
41. Shi, M. et al. Molecular dynamics simulations of the conformational plasticity in the active pocket of salt-inducible kinase 2 (SIK2) multi-state binding with bosutinib. *Comput. Struct. Biotechnol. J.* **20**, 2574–2586 (2022).
42. Shi, M. et al. Interactions between Curcumin and human salt-induced kinase 3 elucidated from computational tools and experimental methods. *Front. Pharmacol.* **14**, 1116098 (2023).
43. Shelley, J. C. et al. Epik: a software program for pK(a) prediction and protonation state generation for drug-like molecules. *J. Comput. Aided Mol. Des.* **21**, 681–691 (2007).
44. Abramson, J. et al. Accurate structure prediction of biomolecular interactions with alphafold 3. *Nature* **630**, 493–500 (2024).
45. Harder, E. et al. OPLS3: A force field providing broad coverage of Drug-like small molecules and proteins. *J. Chem. Theory Comput.* **12**, 281–296 (2016).
46. Friesner, R. A. et al. Glide: A new approach for rapid, accurate Docking and scoring. 1. Method and assessment of Docking accuracy. *J. Med. Chem.* **47**, 1739–1749 (2004).
47. Friesner, R. A. et al. Extra precision glide: Docking and scoring incorporating a model of hydrophobic enclosure for Protein–Ligand complexes. *J. Med. Chem.* **49**, 6177–6196 (2006).
48. Velázquez-Libera, J. L., Durán-Verdugo, F., Valdés-Jiménez, A., Núñez-Vivanco, G. & Caballero, J. LigRMSD: a web server for automatic structure matching and RMSD calculations among identical and similar compounds in protein-ligand Docking. *Bioinformatics* **36**, 2912–2914 (2020).
49. Deng, Z., Chuaqui, C. & Singh, J. Structural interaction fingerprint (SIFt): a novel method for analyzing three-dimensional protein-ligand binding interactions. *J. Med. Chem.* **47**, 337–344 (2004).
50. Phillips, J. C. et al. Scalable molecular dynamics on CPU and GPU architectures with NAMD. *J. Chem. Phys.* **153**, 044130 (2020).
51. Huang, J. et al. CHARMM36m: an improved force field for folded and intrinsically disordered proteins. *Nat. Methods*. **14**, 71–73 (2017).
52. Vanommeslaeghe, K. et al. CHARMM general force field: A force field for drug-like molecules compatible with the CHARMM all-atom additive biological force fields. *J. Comput. Chem.* **31**, 671–690 (2010).
53. Pang, Y. T., Miao, Y., Wang, Y. & McCammon, J. A. Gaussian accelerated molecular dynamics in NAMD. *J. Chem. Theory Comput.* **13**, 9–19 (2017).
54. Miao, Y., Feher, V. A. & McCammon, J. A. Gaussian accelerated molecular dynamics: unconstrained enhanced sampling and free energy calculation. *J. Chem. Theory Comput.* **11**, 3584–3595 (2015).
55. Humphrey, W., Dalke, A. & Schulten, K. VMD: visual molecular dynamics. *J. Mol. Graph.* **14**, 33–38 (1996).
56. Roe, D. R. & Cheatham, T. E. PTRAJ and CPPTRAJ: software for processing and analysis of molecular dynamics trajectory data. *J. Chem. Theory Comput.* **9**, 3084–3095 (2013).
57. Muñoz-Gutiérrez, C., Adasme-Carreño, F., Fuentes, E., Palomo, I. & Caballero, J. Computational study of the binding orientation and affinity of PPAR γ agonists: inclusion of ligand-induced fit by cross-docking. *RSC Adv.* **6**, 64756–64768 (2016).

58. Laskowski, R. A., MacArthur, M. W., Moss, D. S. & Thornton, J. M. PROCHECK: a program to check the stereochemical quality of protein structures. *J. Appl. Cryst. J. Appl. Crystallogr.* **26**, 283–291 (1993).
59. Zuccotto, F., Ardini, E., Casale, E. & Angiolini, M. Through the gatekeeper door: exploiting the active kinase conformation. *J. Med. Chem.* **53**, 2681–2694 (2010).
60. Caballero, J., Morales-Bayuelo, A. & Navarro-Retamal, C. Mycobacterium tuberculosis serine/threonine protein kinases: structural information for the design of their specific ATP-competitive inhibitors. *J. Comput. Aided Mol. Des.* **32**, 1315–1336 (2018).
61. Ferrara, P., Gohlke, H., Price, D. J., Klebe, G. & Brooks, C. L. Assessing scoring functions for protein-ligand interactions. *J. Med. Chem.* **47**, 3032–3047 (2004).
62. Damm-Ganamet, K. L., Smith, R. D., Dunbar, J. B., Stuckey, J. A. & Carlson, H. A. CSAR benchmark exercise 2011–2012: evaluation of results from Docking and relative ranking of blinded congeneric series. *J. Chem. Inf. Model.* **53**, 1853–1870 (2013).
63. Caballero, J. The latest automated Docking technologies for novel drug discovery. *Expert Opin. Drug Discov.* **16**, 625–645 (2021).
64. Wong, C. F. Flexible receptor Docking for drug discovery. *Expert Opin. Drug Discov.* **10**, 1189–1200 (2015).

Author contributions

J.C. carried out the conceptualization of this work. Funding acquisition and project administration were done by J.C. Data curation and calculations were performed by J.L.V.A., E., D.P., and S.A. Visualization and interpretation of models were performed by J.L.V.A. and E., D.P. The writing of the manuscript was done by J.C. All authors reviewed the manuscript.

Funding

This research was funded by FONDECYT Regular grant number 1210138 (JC).

Declarations

Competing interests

The authors declare no competing interests.

Additional information

Supplementary Information The online version contains supplementary material available at <https://doi.org/10.1038/s41598-025-03699-w>.

Correspondence and requests for materials should be addressed to J.C.

Reprints and permissions information is available at www.nature.com/reprints.

Publisher's note Springer Nature remains neutral with regard to jurisdictional claims in published maps and institutional affiliations.

Open Access This article is licensed under a Creative Commons Attribution-NonCommercial-NoDerivatives 4.0 International License, which permits any non-commercial use, sharing, distribution and reproduction in any medium or format, as long as you give appropriate credit to the original author(s) and the source, provide a link to the Creative Commons licence, and indicate if you modified the licensed material. You do not have permission under this licence to share adapted material derived from this article or parts of it. The images or other third party material in this article are included in the article's Creative Commons licence, unless indicated otherwise in a credit line to the material. If material is not included in the article's Creative Commons licence and your intended use is not permitted by statutory regulation or exceeds the permitted use, you will need to obtain permission directly from the copyright holder. To view a copy of this licence, visit <http://creativecommons.org/licenses/by-nc-nd/4.0/>.

© The Author(s) 2025